Please cite as: Journal of Membrane Science, Volume 564, 2018, Pages 218-226
doi: https://doi.org/10.1016/j.memsci.2018.07.028

Comparison of freeze-dried and tape-cast support microstructure on high-flux oxygen transport membrane performance

F. Schulze-Küppers[1,*], U. V. Unije[1], H. Blank[2], M. Balaguer[1,†], S. Baumann[1], R. Mücke[1], W.A. Meulenberg[1,3]

[1] Forschungszentrum Jülich GmbH, Institute of Energy and Climate Research, Materials Synthesis and Processing (IEK-1), 52425 Jülich, Germany

[2] Carl Zeiss Microscopy GmbH, Carl-Zeiss-Straße 22, 73447 Oberkochen, Germany

[3] University of Twente, Faculty of Science and Technology, Inorganic Membranes, P.O. Box 217, 7500 AE Enschede, The Netherlands

Abstract

The overall permeation rate through asymmetric oxygen transport membranes is significantly governed by the porous support. Therefore, the microstructuring of the support's pore structure is essential to achieving the highest performances. Freeze casting is already proven to obtain hierarchical porous structures with low tortuosity, which potentially enhances the oxygen flux of oxygen transport membranes. Although a performance improvement has been reported, such improvement is not self-evident. There has yet to be a detailed comparison of the achieved microstructures in order to identify the relevant microstructural parameters. Asymmetric membranes from $Ba_{0.5}Sr_{0.5}(Co_{0.8}Fe_{0.2})_{0.97}Zr_{0.03}O_{3-\delta}$ consisting of a surface-activated 20 µm membrane layer with tape- or freeze-cast supports that have identical pore volume and layer thickness were manufactured, characterized, and compared by means of oxygen flux measurements. They were also microstructurally investigated via computed X-Ray tomography and flow simulation experiments. In the air/Ar gradient, the freeze-cast support membrane performs below the tape-cast-supported membrane. In particular, the transition zone close to the membrane, which is caused by the freezing process, significantly constrains the diffusivity and permeability of the support, and therefore leads to concentration polarizations. At temperatures below 800 °C, surface exchange kinetics at the membrane-support interface become rate-limiting.

* Corresponding author, tel.: +49 2461 61-6712; fax: +49 2461 61-2455.
Email: f.schulze@fz-juelich.de

† Current address: Instituto de Tecnología Química (Universidad Politècnica de Valencia – Consejo Superior de Investigaciones Científicas), Av. Naranjos s/n, 46022 Valencia, Spain

1 Introduction

Oxygen is one of the most important technical gases and is commonly separated from air by means of large-scale techniques such as cryogenic air separation or pressure swing adsorption. A promising alternative way to separate oxygen from air, particularly on the small and medium scale, is the use of oxygen transport membranes (OTM), which consist of a mixed ionic and electronic conductor (MIEC). In MIEC materials, the oxygen permeation rate increases with temperature and the oxygen partial pressure gradient across the membrane [1]. Consequently, membrane performance is driven by adequate process parameters, such as the use of pressurized air on the feed side and an oxygen-lean sweep gas or vacuum on the permeate side [2].

An additional focus for the potential improvement of OTM performance is the optimization of the membrane architecture. According to Wagner's theory for bulk diffusion process, a reduction of the membrane layers thickness causes an increase in permeation [3], although it also entails a loss in mechanical strength. Consequently, the dense membrane layer must be supported by a porous scaffold that provides the mechanical stability in an asymmetric membrane [4]. The improvement of the permeation rate by asymmetric membranes has already been demonstrated for different membrane materials [5, 6, 7].

The resulting architectures offer various advantages in comparison to bulk membranes, for example higher permeation and the possibility of using more chemically stable membrane materials which usually possess lower oxygen permeability [8, 9, 10].

However, a non-adequate support microstructure becomes rate-limiting for gas transfer. The gases might accumulate or deplete at the membrane-support interface, which leads to a lower p_{O2} gradient, i.e. driving force, across the membrane layer itself. Such concentration polarization therefore lowers the overall membrane performance [6, 11, 12, 13, 14, 15], which becomes more important the higher the flux is.

Accordingly, a microstructural optimization of the porous support architecture is required, which involves controlled and tailored porosity, including pore tortuosity, morphology, and opening diameter [14]. Novel fabrication methods, for example freeze casting [16, 17, 18, 19, 20, 21], phase-inversion casting [9, 22, 23], inkjet printing [24], and their combinations are currently being investigated to supply and optimize this sort of asymmetric microstructure. Among the methods mentioned, freeze casting has already proven to obtain hierarchical porous structures that potentially enhance the oxygen flux of the membrane [17, 23]. Although a performance improvement has been reported, there has yet to be a detailed comparison of the achieved microstructures in order to identify the relevant microstructural parameters.

Therefore, in this study, the effect of freeze-dried and tape-cast support microstructures on oxygen transport through the asymmetric membrane is investigated using $Ba_{0.5}Sr_{0.5}(Co_{0.8}Fe_{0.2})_{0.97}Zr_{0.03}O_{3-\delta}$ (BSCF3Zr) as membrane material. The advantage of BSCF3Zr is that the high oxygen permeability minimizes the bulk diffusion resistance and, thus, uncovers bottlenecks caused by other transport mechanisms such as an insufficient support microstructure or limited oxygen surface exchange. By substituting $Ba_{0.5}Sr_{0.5}Co_{0.8}Fe0_{.2}O_{3-\delta}$ (BSCF) with 3 mol% Zr on the B-site, the degradation of oxygen flux – related to the phase transformation from cubic to hexagonal perovskite at temperatures below 850 °C – is partly suppressed [25, 26]. This enables a more reliable measurement of oxygen flux to study oxygen transport at this temperature range. Membranes were manufactured by a water-based freeze-casting process. The microstructural parameters - support, membrane, and activation layer thicknesses as well as support porosity - were subsequently mimicked using tape casting. Oxygen permeation rates are measured and limiting processes identified. Since the reproducibility of freeze-dried structures is limited [27], the real microstructures were thoroughly analyzed in 3D, on the same samples used for permeation measurement, and their effect on oxygen transport is studied computationally. The identification of limiting processes in combination with the detailed

microstructure analysis enables a straight-forward development of improved support microstructures for oxygen transport membranes.

2 Experimental

Asymmetric membrane fabrication:
The $Ba_{0.5}Sr_{0.5}(Co_{0.8}Fe_{0.2})_{0.97}Zr_{0.03}O_{3-\delta}$ (BSCF3Zr) ceramic powder was commercially provided by Treibacher Industrie AG, Austria. The powder exhibits a monomodal particle size distribution with d_{10} ~1.7 µm, d_{50} ~3.6 µm, and d_{90} ~5.9 µm, as determined by dynamic light scattering (Horiba LA 950V2). The specific surface area is 1.4 m^2/g, as determined by nitrogen adsorption (Areamat, Jung Instruments, Germany) analyzed using the BET method.
The asymmetric membranes were fabricated either by sequential tape casting (TC) or freeze casting (FC) of the porous support and a subsequent screen printing of the membrane layer. For tape casting, the BSCF3Zr powder was dispersed in an azeotropic mixture of ethanol and methyl ethyl kethone using Nuosperse® FX9086 (Elementis Specialties, Inc.) as a dispersing agent. Polyvinyl butyral (Butvar® PVB B-98, Solutia Inc.) was added to this mixture as a binder; Solusolv® 2075 (Solutia Inc.) and PEG400® (Merck) as plasticisers. The preparation of the slurries followed the procedure described in [7, 28]. In a first step, the thin membrane layer was cast on a polymer foil with a 50 µm doctor blade gap using a slurry without pore former. After drying this thin membrane layer, the porous support was cast on top with a doctor blade gap of 2.25 mm. Corn starch Cargill C-Gel (Cargill, Germany) with a particle size range of 2–30 µm was then used as a pore-forming agent. The support slurry contains 40.5 wt% corn starch, which leaves the porosity after burn out. For shaping, the specimens were cut out from the dried green tape, debindered, and subsequently co-fired in air at 1130 °C for 5h.
Porous supports were prepared using the freeze-casting technique. A water-based suspension containing the BSCF3Zr ceramic powder and organic additives, i.e. binder (PEG4000S, Clariant) and dispersant (Dolapix C64, Zschimmer & Schwarz GmbH&Co), was prepared and mixed in a planetary mixer for blending and homogenization. The slurry was cast into a cylindrical Teflon mold with an aluminum base plate and subsequently cooled to -50 °C using a Martin Christ Epsilon 2-4 lyophilizer. The sublimation of ice crystals took place after complete freezing at -55 °C and 0.1 mbar pressure for 24 hours, with a final drying step at +30 °C at the same pressure. Such green supports were pre-sintered in air at 1050 °C, with a 3-hour dwell time, followed by the grinding of the support surface at the air side. The dense BSCF3Zr membrane layer was screen-printed on the unground BSCF3Zr support side, which was in contact with the polished aluminum base plate. On this side, ice crystal nucleation starts to entail a fine porous region with randomly oriented pores, which simplifies the covering of pores with the screen-printed layer. The organic suspension for the BSCF3Zr dense coating contains a solvent (terpineol, Sigma-Aldrich, Germany) and a binder (ethylcellulose 46 cP, Sigma-Aldrich, Germany). The final sintering step was performed at 1130 °C in air for 5 hours.
The oxygen activation layer was screen-printed on the top of the already sintered membrane using a sieve with a 15 µm wet layer thickness and the same BSCF3Zr paste as used for the dense layer. These layers were only sintered at 1000 °C for 1h in order to keep the layer porous but well attached to the membrane surface.

Microstructure analysis:
Scanning electron microscopy of the polished membrane cross sections was performed with a Zeiss Ultra 55 and a FEI Phenom. Quantitative image analysis was conducted using the commercial software analySIS pro (Olympus Soft Imaging Solutions GmbH, Germany).

3D microstructure analysis was performed by X-ray computed tomography (XCT) on the BSCF3Zr membranes after permeation measurements. These were embedded in resin by vacuum impregnation to protect the porous structure prior to cutting. Cylindrical samples with a diameter of 1 mm and a height of 0.95 mm were cut. A Zeiss Xradia 520 Versa X-ray microscope with a tungsten transmission target was used. Scanning of the TC sample was performed at a voltage of 140 kV using an HE2 filter. The FC sample was scanned at a voltage of 120 kV using an HE1 filter. Each tomography was acquired with an X-ray source power of 10 W, 20x optical magnification, the binning 2 setting of the 4 Megapixel CCD camera, and an exposure time of 26 s for each radiograph – with 3001 radiographs being taken over 360°. The recorded data was reconstructed using a Feldkamp–Davies–Kress [29] algorithm, giving a final reconstructed voxel size of 0.451 µm. For the 3D model, membrane und support material were separated from the pores by a threshold using the GeoDict 2017 software (Math2Market GmbH, Germany).

Oxygen permeation test:

Permeation measurements were performed on a double chamber quartz glass reactor. Membranes consisted of gastight 14.7 mm diameter discs, which were placed between two quartz glass tubes and sealed by two gold rings with an inner diameter of 13 mm. On the porous support side of the membrane, oxygen (200 mL/min) or ambient air (250 mL/min) were used as a feed gas, while argon (50 mL/min) was used as a sweep gas on the dense membrane side. After three hours equilibration, the permeate gas was analyzed using a mass spectrometer (Pfeiffer OmniStar) following the species Ar, O_2, and N_2. The permeation rates ($mL \cdot min^{-1} \cdot cm^{-2}$) were calculated by dividing the oxygen mass flow rate in the permeate gas by the effective surface area (1.33 mm^2) of the membranes. Appropriate sealing was confirmed by measuring the nitrogen tracer content of the permeate stream. The calculated oxygen leak flux was always lower than 1% compared to the permeated oxygen flux. The performance of the membranes was measured as a function of temperature and oxygen partial pressure in the feed gas, i.e. ambient air (p_{O2} = 0.21 bar) and oxygen (p_{O2} = 1 bar).

3 Results and Discussion

3.1 Membrane performance

Oxygen flux through asymmetric membranes is highly dependent on its geometric properties, such as membrane-, support-, and activation layer thickness as well as the porosity. In this study, these parameters were intentionally kept equal for both membrane assemblies. Figure 1 shows the polished cross sections of the two measured membranes. The aim was to reduce the concentration polarization, known from tape cast supports, by freeze casting. Due to the straight channel structure of freeze cast supports, an improvement in gas transport compared to the tape cast support was expected. The support microstructures, both with a thickness ($L_{support}$) of 990–1000 µm and a total porosity of approx. 45 % were prepared by freeze casting (FC) and tape casting (TC), respectively. The membrane layer thickness ($L_{mem.layer}$) of both membranes was 22-24 µm. This is well below the characteristic thickness L_c for the comparable material BSCF [30, 31, 32], which is expected to be very similar to the unknown L_c of BSCF3Zr. The L_C of a material, i.e. the ratio between the oxygen self-diffusion coefficient and the surface exchange coefficient [33], reflects the thickness at which the bulk diffusion and the surface exchange contributions to the overall permeation are equal. In order to facilitate oxygen surface exchange, the surface area of the membrane is increased by a porous activation layer of the same material with a 4–6 µm thickness ($L_{act.layer}$) in both cases.

While tape casting results in uniform support porosity and pore size (Figure 1 A), freeze cast samples possess a large gradient in porosity and pore size along the thickness (Figure 1 B). For freeze casting, a suspension is frozen in a container with a cooled base plate. The ceramic particles are repelled by the growing ice crystals and form the pore walls, while after sublimation of the ice crystals the pores are formed (ice-templating). At the beginning of the freezing process, at the interface between the cooled base plate and the suspension, the first fine crystallization nuclei occur, which lead to a chaotic, finely porous pore structure. This so-called transition zone depends on the freezing conditions and might be helpful to increase the specific surface area facilitating surface exchange reactions. Finally this microstructure differs completely from microstructures obtained by tape casting as shown in **Figure *1***.

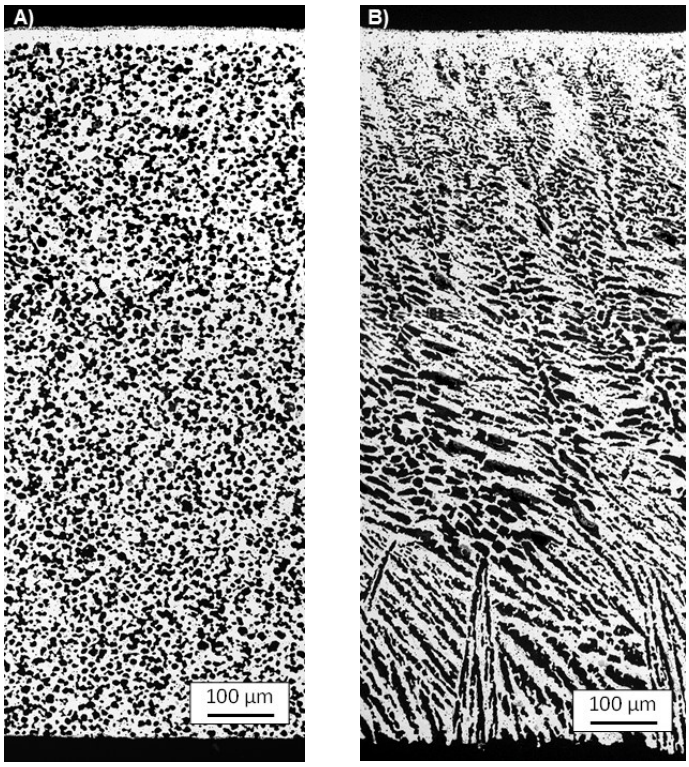

Figure 1: *Cross sections of the membranes after permeation measurement. A) membrane with TC support and B) membrane with FC support.*

Oxygen transport in MIEC materials is well-understood and can be described for small p_{O2}-gradients by the extended Wagner Equation (1), which considers both solid state diffusion and oxygen surface exchange kinetics:

$$j_{O_2} = \frac{1}{L \cdot \left(1 + \frac{2L_c}{L}\right)} \cdot \frac{RT}{4^2 F^2} \int_{p''_{O_2}}^{p'_{O_2}} \sigma_{amb} d \ln p_{O_2} \qquad (1)$$

where j_{O2} is the oxygen permeation rate, R the gas constant, F the Faraday constant, *L* the membrane thickness, L_c the characteristic thickness, σ_{amb} the ambipolar conductivity, and p'_{O_2} and p''_{O_2} the oxygen partial pressures at the two membrane surfaces [1, 3, 12].

Figure 2(A) shows the oxygen permeation rates of the two asymmetric membranes in an air/Ar-gradient in comparison with a 1 mm disc membrane. The porous support was placed at the feed side. Taking into account the temperature-dependent L_c (i.e. 20 µm at 900°C and 147 µm at 750 °C) values determined experimentally by [30] for the parent compound BSCF in an air/He gradient, the oxygen flow would increase, according to (1), by a factor of 42 at 900 °C and a factor of 28 at 750 °C when the membrane thickness is reduced from 1 mm to 22 µm. However, above 800 °C, both supported membranes (L = 22 µm) have an increase in oxygen permeation rate only by factor 1.5–2.3.

The increase in oxygen permeation using pure oxygen as feed gas (see **Figure *2***(B)) compared to the air/Ar p_{O2}-gradient is attributed to the elimination of concentration polarizations inside the support. This means that nitrogen cannot accumulate at the support–membrane interface lowering the driving force for the solid-state diffusion process in the membrane layer itself [14, 34]. Oxygen as feed gas has an enhancement factor of 8 at around 1000 °C and a factor of 5 at around 750 °C for oxygen permeation, compared to the measurement in air/Ar gradient. However, the apparent driving force, calculated from the p_{O2} at both membrane sides remains the same at 1000°C and only increases slightly by a factor of 1.15 at 750 °C. This is still well below the predicted increase according to Equation (1), which does not consider transport through the support.

Furthermore, the measurements in air/Ar and O_2/Ar oxygen partial pressure gradients, with the support at the feed side, only revealed a minor influence of support type on the oxygen permeation rate. The permeation enhancement ($j_{O_2}^{improvement}$) through a supposedly lower tortuosity for the FC support [10] with its hierarchical architecture is calculated from the oxygen permeation through the FC membrane ($j_{O_2}^{FC}$) and the TC membrane ($j_{O_2}^{TC}$) and depicted as inlet inside the graphs in Figure 3.

$$j_{O_2}^{improvement} = \frac{j_{O_2}^{FC} - j_{O_2}^{TC}}{j_{O_2}^{TC}} \cdot 100 \qquad (2)$$

An improvement in oxygen permeation by using a FC support was not observed for the in-air measurement (see Figure 2(A) inlet). When pure oxygen is used as a feed gas, the use of an FC support is slightly beneficial at temperatures > 850 °C, as depicted in the inlet of Figure 2(B).

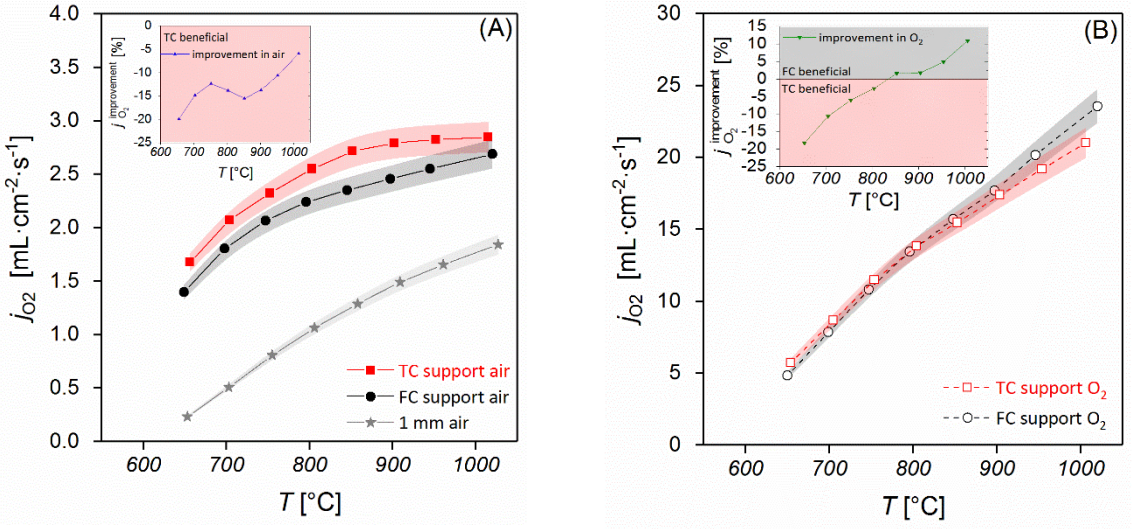

Figure 2: *Comparison of oxygen permeation through asymmetric membranes with tape-cast (TC) and freeze-cast (FC) support for in air and pure oxygen feed gas. An estimated measurement error of ± 5% is depicted as the error interval.*

An indicator for predominant transport mechanism through the membrane is the activation energy E_A, which can be calculated from the slope of the permeance in an Arrhenius plot. The permeance J_{O_2} is defined as the normalized oxygen flux j_{O_2} by the driving force [35]. The permeance is necessary to consider because in the measurements, the oxygen partial pressure at the sweep side is determined by the enrichment of the sweep gas with the permeated oxygen and, hence, is temperature dependent. For solid-state diffusion limitation, $E_{A\ bulk(1000\text{-}800°C\ )}$= 45 kJ/mol was calculated from the permeance of the 1 mm thick BSCF3Zr membrane disc (see Figure 2), assuming negligible surface exchange limitation. This value is in good agreement with BSCF measurements reported by Shao et. al. [36]. For comparison, calculating the activation energy on basis of the oxygen permeation, $E^{app}_{A\ bulk(1000\text{-}800°C\ )}$ is 29 kJ/mol.

However, in our case, the exact driving force across the membrane layer cannot be determined due to the presence of the porous support. Moreover, the gaseous transport through the support pores possesses a different driving force term, i.e. p'-p'' instead of $ln\frac{p'_{O_2}}{p''_{O_2}}$. Therefore, after all we decided to use the permeation rate instead of the permeance to calculate an apparent activation energies E_A^{app}, because a change in transport mechanism still is reflected by a change in E_A^{app} making qualitative discussions possible.

Usually, a significantly lower apparent activation energy compared to bulk diffusion (here 29 kJ/mol) indicates limitations by gas transport inside the support ($E^{app}_{A\ support}$), whereas a significantly higher value indicates limitations by surface exchange reactions ($E^{app}_{A\ surface}$).

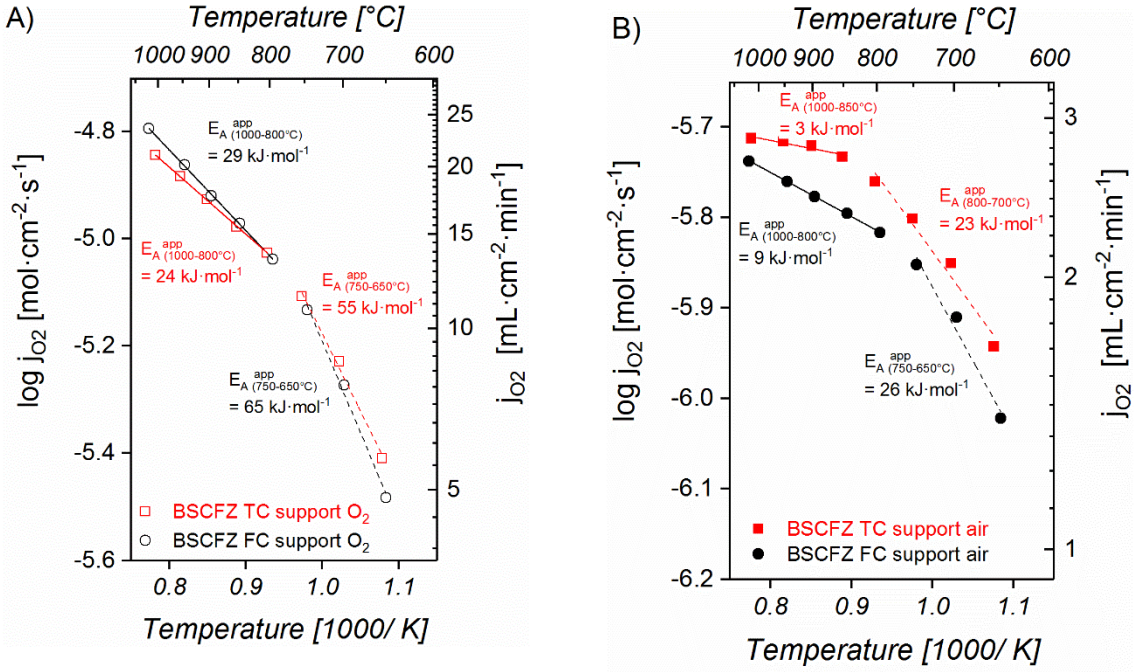

Figure 3: *Arrhenius plot of oxygen permeation of the TC- and FC-supported membranes with activation layers using A) O_2 and B) air as a feed gas on the support side.*

The E_A^{app} of the asymmetric membranes changes with temperature, indicating a change in the limiting transport mechanism. Using pure **O_2 as a feed gas** (Figure 3A) on the support side diminishes concentration polarizations in the porous support. Only an absolute pressure drop lowers the oxygen partial pressure at the membrane layer, which is much less compared to the concentration polarizations. Consequently, The E_A^{app} above 800 °C is close to that of solid-state diffusion, indicating no surface exchange limitations. Below 800 °C, E_A^{app} increases significantly for the FC-supported

($E_{A\,(750\text{-}650°C)}^{app}$ = 65 kJ/mol) and TC-supported ($E_{A\,(750\text{-}650°C)}^{app}$ = 55 kJ/mol) membranes because the surface exchange kinetics are no longer negligible. This is due to the temperature dependence of the L_c, which for instance for BSCF increases significantly from 20 µm at 900 °C to 147 µm at 750 °C. The difference in $E_{A\,(750\text{-}650°C)}$ between the two asymmetric membranes might be caused by a different specific surface area inside the support close to the membrane layer.

In contrast, using **air as a feed gas** (Figure 3 (B)), the $E_{A\,(1000\text{-}850°C)}^{app}$ is significantly lower above 850 °C, i.e. 3 kJ/mol for the TC-supported membrane, which strongly indicates severe gas transport limitation inside the support pores. Between 700 °C and 800 °C, the $E_{A\,(700\text{-}800°C)}^{app}$ is close to that of solid-state diffusion and appears to be even larger at lower temperatures, although the single data point at 650 °C cannot be used for quantification. Nevertheless, it is reasonable to assume an important contribution of at least two mechanisms: gas diffusion in the support and solid-state diffusion in the membrane layer. It is also possible that surface exchange has a considerable impact at low temperatures.

The FC-supported membrane shows $E_{A\,(1000\text{-}800°C)}^{app}$ of 9 kJ/mol and $E_{A\,(750\text{-}650°C)}^{app}$ of 26 kJ/mol for the high and low temperature regions, respectively, and, hence a similar trend. The latter is higher compared to the TC support, which is in agreement with the hypothesis of non-negligible surface exchange contributions at the support–membrane interface and a possibly higher surface area in that part of the FC-support compared to the TC-support. At higher temperatures, the $E_{A\,(1000\text{-}800°C)}^{app}$ is larger compared to the TC support, indicating lower support resistance as expected from lower tortuosity obtained by freeze casting. At the same time, the oxygen permeation rate is lower, which is contradictory to that.

These results reveal the necessity of a more detailed analysis of the support microstructure and its effects on gas transport.

3.2 Detailed microstructure analysis

Besides porosity (ε), tortuosity (τ) and pore opening diameter (d_{50}) are important pore structure parameters for evaluating the gas transport through porous supports [37, 38]. In addition, the specific surface area ($A_{spec,support}$) inside the support close to the membrane is crucial for surface exchange reactions [14]. For a detailed analysis of that features, computed X-ray tomography (XCT) was performed (Figure 4).

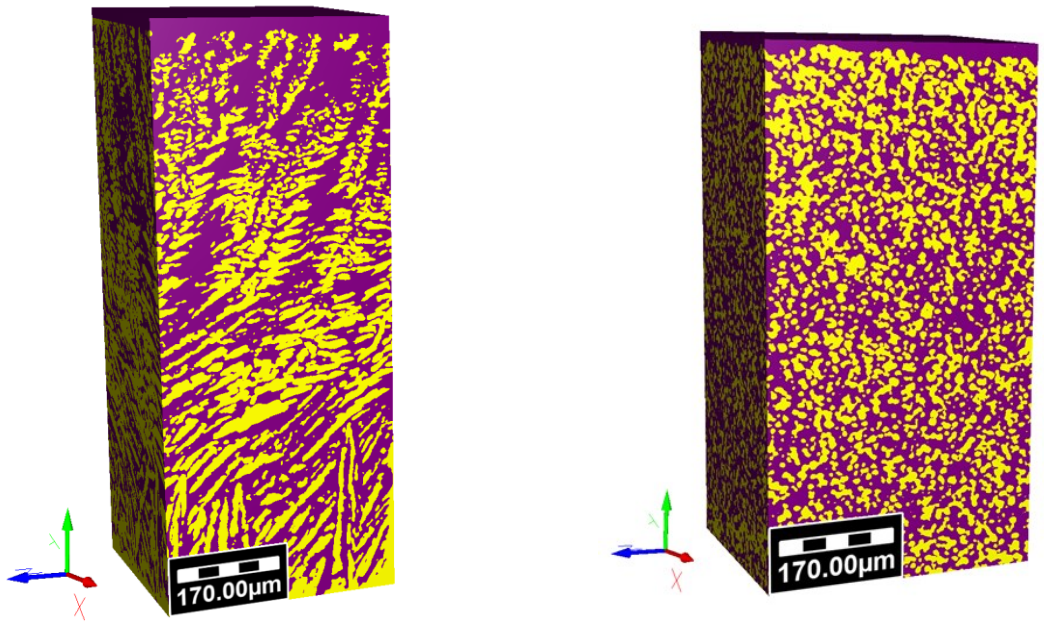

Figure 4: *Support architecture of a freeze-cast (FC) (left) and tape-cast (TC) (right) asymmetric membrane, reconstructed from XCT data (porosity = yellow). The membrane layer is located at the top.*

Table 1: *Comparison of averaged microstructural parameters of tape-cast (TC) and freeze-cast (FC) asymmetric membranes.*

Sample name	$L_{act.layer}$ [µm]	$L_{mem.layer}$ [µm]	$L_{support}$ [µm]	$\varepsilon_{support-mean}$ (quantitative SEM-image analysis) [%]	d_{50} (XCT) [µm]	τ (XCT) [-]	$A_{spec.support}$ (XCT) [m^2/cm^3]
TC	5–6	22–24	990	45.5 ± 1.8	5.0	1.7	0.21
FC	4–5	22–24	1000	45.5 ± 5.5	6.8	1.8	0.16

The structural parameters, such as tortuosity (τ), average pore opening diameter (d_{50}), specific surface area ($A_{spec.support}$), and porosity (ε) provide an overview description of the support and are summarized in Table 1. It should be noted that the determination of porosity from XCT data only detects pores above the voxel sizes of 0.451 µm. However, the results are in good agreement with the values of quantitative image analysis. However, these are only averaged values across the entire support thickness – a detailed description of the microstructure as a function of the position in the support is evaluated in different segments along the support height from the XCT data (y-axis in **Figure 4**). Since the TC support is very uniform, only four segments were evaluated while the FC support is divided into 12 segments due to the much higher inhomogeneity.

Specific surface area

The surface area on the membrane sweep side is identical for both membrane types due to the porous surface enhancement layer being manufactured with identical parameters and materials. In contrast, the specific surface area at the membrane–support interface requires detailed investigation.

The FC support possesses an average specific surface area ($A_{spec.support}$) of 0.16 m^2/cm^3, which is 24 % lower compared to the TC support (0.21 m^2/cm^3). Due to the varying porosity and pore diameters, the specific surface area changes along the FC support thickness, as shown in Figure 5.

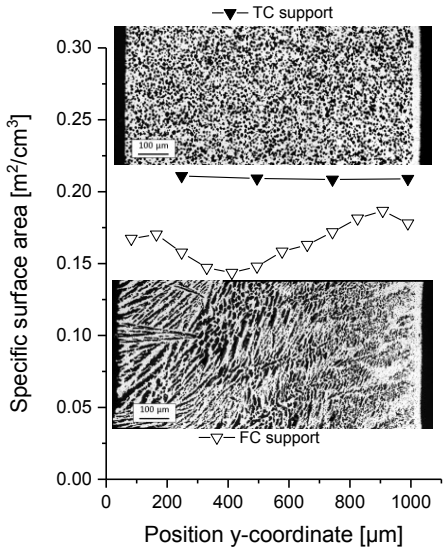

Figure 5: *Specific surface area vs. section position (y-coordinate), where 0 µm is the support-feed side without membrane layer and 1000 µm is the position of the interface to the membrane layer. Inlet: SEM cross section of the corresponding membranes.*

Tortuosity

Tortuosity is important for describing the path length of a molecule through a pore channel (L_{pore}) compared to the shortest length through the support ($L_{support}$), as given in equation (3).

$$\tau = \frac{L_{pore}}{L_{support}} \tag{3}$$

The TC porous support possesses randomly shaped pores with tortuosity, which depends on the pore volume and percolation of the pore network and is caused by the burnout of a pore-former (in this case, corn starch). Using freeze casting for support manufacturing, the ice crystals grown are used as the template for the pores.

The average tortuosity, calculated from XCT, for the non- optimized FC support is 1.8 and thus nearly the same as for the TC support (1.7). However, while the tortuosity of the TC support does not vary across the support thickness, the FC support exhibits increasing tortuosity from 1.2 on the support–gas side, and up to 1.9 at the support–membrane interface, as can be seen from Figure 6. The variation in porosity is caused by the zone in which ice crystals nucleate and start to grow. The orientation of the ice crystals gradually aligns, with the distance from this nucleation zone, to the freezing direction [39]. Resulting in a high tortuosity in the nucleation zone, close to the membrane layer, and lower tortuosity at the opposite side.

For gas diffusion processes through porous media the tortuosity factor, i.e. tortuosity squared $\kappa=\tau^2$, must be considered. As shown in **Figure 6** this increases the discrepancy between the two supports.

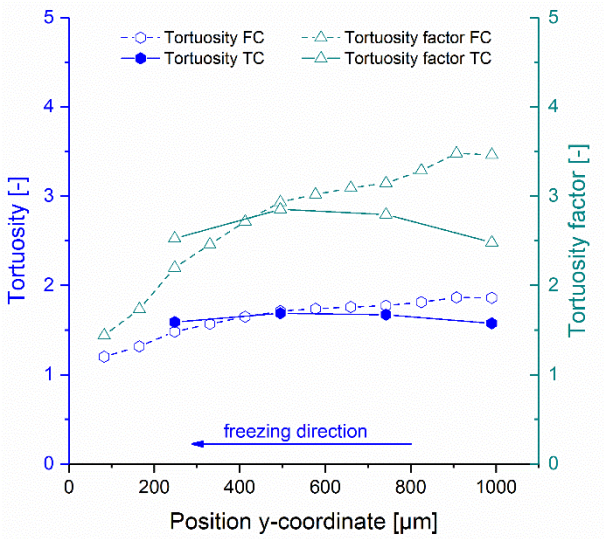

Figure 6: *Evolution of tortuosity (τ) and tortuosity factor ($\kappa=\tau^2$) plotted vs. section position (y-coordinate), where 0 is the support side and 1000 the position underneath the membrane layer.*

Porosity and pore opening diameter

Both support porosities show a good connectivity of the pores, indicating that nearly all pores contribute to gas transport. The share of closed porosity is negligible: 0.04 % for TC and 0.09 % for FC supports. The pores have an irregular variation in shape, size and diameter. Calculating an average pore diameter is a simplification of the real pore structure, but is necessary to identifying the main transport mechanisms of gas transport inside the porous support. As intended, both support types possess identical average porosities of 45 %. Nevertheless, the porosity of the TC support is homogenous across the support thickness, whereas the FC support shows an unintended porosity gradient (**Figure 7**). The reason for this is again the growth and shape of the ice crystal templates. The membrane layer was printed on the nucleation side, where ice crystal growth starts and the porosity and pore diameter are at their lowest. The average support porosity is 45 %, gradually decreasing from 55 % on the support–air side (y=0 µm) to 32 % close to the membrane layer (y=1000 µm), as shown in Figure 6.

The average pore opening diameter (d_{50}) for each segment was calculated from the XCT data computationally using the liquid intrusion porosimetry method and the GeoDict software. The average d_{50} of FC support is 6.8 µm, only slightly larger than for TC supports with 5 µm. However, porosity and the pore size of the TC support are homogeneously distributed, while the FC support again possesses a gradient along the height.

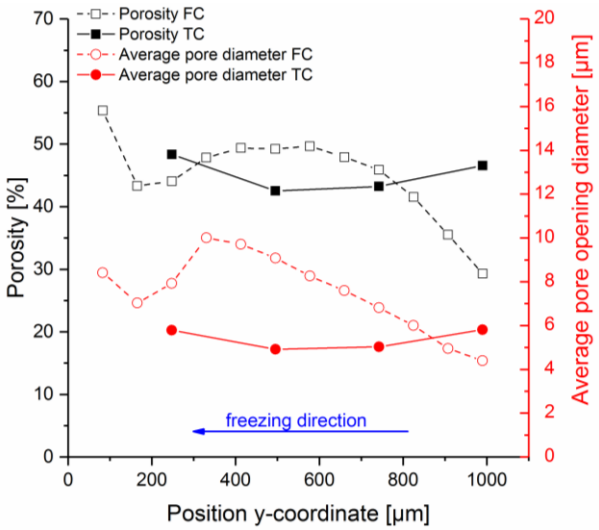

Figure 7: *Evolution of porosity (ε) and average pore opening diameter (d_{50}) plotted vs. section position (y-coordinate), where 0 is the support side and 1000 the position underneath the membrane layer.*

3.3 Discussion of support microstructure influence on gas transport

Figure 3 showed a change in the transport mechanism when switching the feed gas from air to O_2. When using air, the performance of the FC supported membrane was worse than that of the TC supported membrane, while the use of the FC support became advantageous for O_2-feed above 800 °C. This enhancement is an indicator for the larger concentration polarization inside the FC support, contrary to expectations. This revealed the necessity of a deeper computational analysis of the support microstructure's influence on the different transport mechanisms. In addition to the average pore opening diameter d_{50} (cf. **Figure 7**), the permeability B_0 – reflecting viscous flow – and the effective diffusivity D^{eff} – reflecting gas diffusion – were determined for both supports.

Gas permeability (viscous flow) was computed by a virtual flow experiment solving the Navier–Stokes equation, assuming laminar flow and according to that a pressure difference of 0.02 Pa. The permeability B_0 is determined by Darcy's law:

$$Q = \frac{-B_0 A}{\mu}\frac{\Delta p}{L} \tag{4}$$

where Q is the flow rate, B_0 the intrinsic permeability of the medium, A the cross-sectional area to flow, μ the viscosity, Δp the pressure drop, and L the length. The computed permeability is a material property independent of fluid viscosity or pressure drop. The boundary condition was taken to be Dirichlet (symmetric) in order to avoid an artificial increase of the flow path.

For gas diffusion at 900 °C (effective diffusivity), the support was modeled by continuum mechanics, solving Laplace's equation in pores with the application of the Neumann boundary condition on the pore/solid boundaries [40]. The effective diffusivity (Equation (5)) describes the effect of support pore space geometry on diffusion:

$$D^{eff} = D_{ij} \cdot \frac{\varepsilon}{\kappa} \tag{5}$$

where ε is the support porosity and $\kappa=\tau^2$ the tortuosity factor, according to Norman Epstein [41]. Gas permeability and the effective diffusivity factor are plotted in Figure 8 as a function of the position inside the support (y-coordinate).

The simulation shows an almost constant gas permeability and effective diffusivity factor for the TC support, while the values for the air side (position 0) of the FC support are higher and deteriorate significantly along the support thickness. At the support position between 700 µm and 800 µm, gas permeability and the effective diffusivity factor values drop below those of the TC support, where the TC support starts to perform better. The transition in gas exchange performance is caused by the change in microstructure at the nucleation zone of the FC support, onto which the membrane layer was screen-printed. In this zone, porosity and average pore diameter are lower than for the TC support (cf. **Figure 7**), forming bottlenecks for gas exchange between neighboring pores and leading to concentration polarizations inside the support. This explains that the microstructure of this FC support (with its transition zone) is less suitable for diffusive gas transport than the TC carrier.

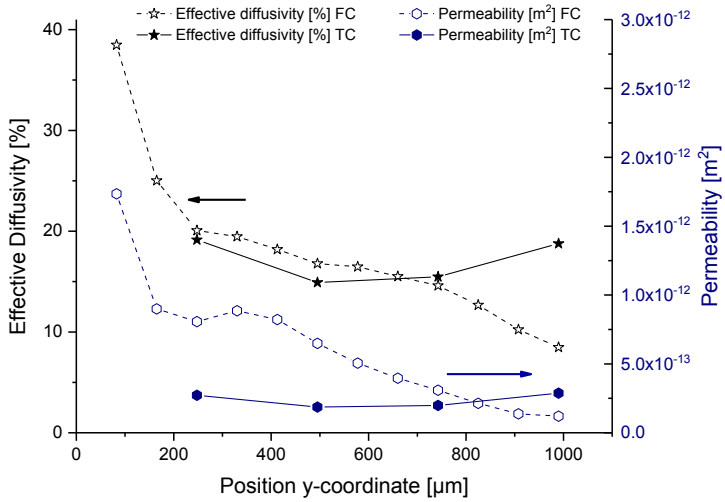

Figure 8*: The evolution of effective diffusivity and gas permeability at 900 °C plotted vs. section position (y-coordinate) where 0 is the support feed gas side and 1000 the position underneath the membrane layer on the sweep gas side.*

How large the pore diameter must be in order to accelerate the gas transport in the pores can be determined by the relationship between the mean path length of the oxygen and nitrogen molecules ($\bar{l}$) and the average pore diameter (d_{50}). The predominant diffusion mechanism depends on the relation between the average pore diameter and the mean free path length of the gas molecules. Therefore, oxygen transfer in porous supports is dominated by Knudsen diffusion for a relation of $\bar{l}/d_{50} > 10$ and by molecular diffusion for $\bar{l}/d_{50} < 0.01$ with a transition zone in-between, where Knudsen and molecular diffusion occur at the same time [42]. The mean free path length is calculated for a pressure of 1 bar, according to [43] in Equation (6):

$$\bar{l} = \frac{kT}{\pi\sqrt{2}d^2p} \qquad (6)$$

where k=Boltzmann constant, *T*=absolute temperature, *d*=kinetic diameter of the gas molecule, and *p*=absolute pressure. For molecular oxygen and nitrogen with a kinetic diameter of 0.346 nm and 0.364 nm respectively [44], the mean free path length is calculated at 900 °C and plotted into Figure 9. According to the $\bar{l}/d_{50}$ ratios, the boarders for the different gas transport mechanisms are plotted in Figure 9 versus the pore opening diameter. The predominant transport mechanism results from the intersections of the mean free path lengths of the gases, i.e. O_2 and N_2, and the pore diameter of the FC support at both sides of the nucleation zone, i.e. positions 700 µm and 1000 µm.

For example, Knudsen and molecular diffusion occur in parallel (transition zone) inside the nucleation zone of the FC support (d_{50}=7 µm at the 700 µm position down to d_{50}=4 µm at the 1000 µm position cf. **Figure 7**). The same applies to the TC support with a uniform d_{50} of 5 µm. The smaller the average pore diameter is, the more the gas transport is shifted in direction of Knudsen diffusion, which in turn increases concentration polarizations inside the support.

Summarizing, the gas transport in the FC support is slowed down on the one hand by the even smaller d_{50} of the pores and also by the lower porosity of the nucleation zone, compared to the TC support. At the same time, the hypothesis of enhanced specific surface area in the nucleation zone potentially facilitating surface exchange did not apply (**Figure 5**).

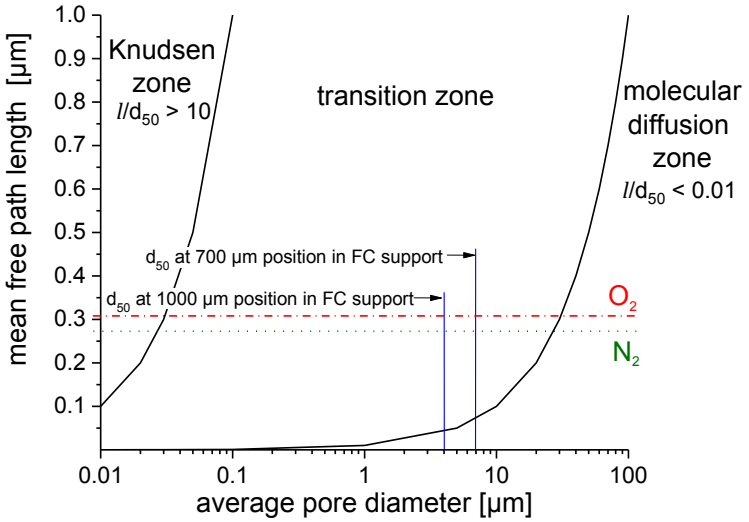

Figure 9: *Predominating gas transport process depending on pore diameter at 900 °C.*

In order to accelerate the diffusion process, the pore diameter of support should be, in general, well above 20 µm so as to facilitate the molecular diffusion, as can be seen from the minimum pore diameter at which molecular diffusion dominates in Figure 9. In addition, this pore size could enable viscous flows as a further transport mechanism and thus an improved gas exchange in the support, as has already been shown in simulations [15]. Taking both the local pore diameters and the pore size distribution over the entire support into account, it is evident that neither the TC nor the FC support has pores with sufficient large opening diameters to only facilitate molecular diffusion (cf. Figure 10). Even the positive effect of a higher ratio of large pores in the FC support compared to the TC support is tarnished by the fine porous transition zone originated during the freezing process. A freeze-cast support, in the configuration investigated here, is therefore not an option for overcoming gas-phase polarization inside the support. Pore opening diameters >20 µm and the avoidance of a transition zone when using the freeze-casting technique are recommended for improved support microstructures, which appears to be technically possible [45].

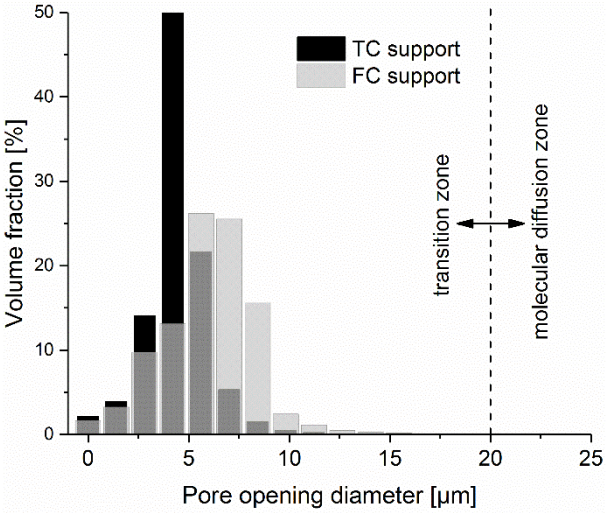

Figure 10: *Pore diameter distribution of freeze- and tape-cast supports.*

4 Conclusion

Asymmetric membranes promise an increase in oxygen flux compared to bulk membranes. However, state-of-the-art supports, such as those obtained by tape casting, can restrict gas transport and therefore lower the driving force for the oxygen flux across the membrane layer significantly. Novel processing routes leading to pore channels with lower tortuosity and larger pore opening diameters have been proven to enhance the flux, but a detailed investigation of the microstructural parameters had yet to be made. Therefore, asymmetric membranes of the same thickness with identical porosity were manufactured by means of tape and freeze casting. A comparison of the oxygen flux of these membranes revealed no improvement using a freeze-cast support. In principle, the hierarchical microstructure of the freeze-cast support enhances gas transport capability. However, particularly the nucleation and transition zone originated by the freezing process, where the membrane layer was screen-printed, strongly constrains diffusivity due to insufficient porosity and pore opening diameters. This leads to a more pronounced concentration polarization inside the freeze-cast support compared to the tape-cast support. As a result, the oxygen permeation of the FC-supported membrane did not exceed that of the TC-supported membrane. The pore opening diameter of both supports indicates molecular and Knudsen diffusion occurring in parallel.

It should be noted that these findings were achieved using a non-optimized freeze cast support. Increasing the pore opening diameters above 20 µm will enhance the gas transport capability of the support. This can definitely be achieved using freeze casting or other advanced manufacturing processes such as phase-inversion casting using optimized parameters. Once optimized and reproducible support structures are available, further reductions in membrane layer thickness together with surface activations can be expected to further increase oxygen permeation.

5 Acknowledgement

We are grateful for the financial support we received from the European Commission in the framework of the GREEN-CC Project (Grant Agreement no. 608524). The authors would also like to thank Mr. Stefan Heinz for his support in performing the permeation measurements.

1 P.-M. Geffroy, E. Blond, N. Richet, T. Chartier, Understanding and identifying the oxygen transport mechanisms through a mixed-conductor membrane, *Chem. Eng. Sci.* 162 (2017) 245-261.

2 A.C. Bose, Inorganic Membranes for Energy and Environmental Applications, Springer, New York, 2009.

3 C. Wagner, Equations for transport in solid oxides and sulfides of transition metals, Prog. *Solid State Chem.* 10 (1975) 3-16.

4 S. Baumann, W.A. Meulenberg, H.P. Buchkremer, Manufacturing strategies for asymmetric ceramic membranes for efficient separation of oxygen from air, *J. Europ. Ceram. Soc.* 33 [7] (2013) 1251-1267.

5 S. Baumann, J.M. Serra, M.P. Lobera, S. Escolástico, F. Schulze-Küppers, W.A. Meulenberg, Ultrahigh oxygen permeation flux through supported $Ba_{0,5}Sr_{0,5}Co_{0,8}Fe_{0,2}O_{3-\delta}$ membranes, *J. Membr. Sci. 377* (2011) 198-205.

6 F. Schulze-Küppers, S. Baumann, W.A. Meulenberg, D. Stöver, H.-P. Buchkremer, Manufacturing and performance of advanced supported $Ba_{0,5}Sr_{0,5}Co_{0,8}Fe_{0,2}O_{3-\delta}$ (BSCF) oxygen transport membranes, *J. Membr. Sci.* 433 (2013) 121-125.

7 F. Schulze-Küppers, S. Baumann, F. Tietz, H.J.M. Bouwmeester, W.A. Meulenberg, Towards the fabrication of $La_{0.98-x}Sr_xCo_{0.2}Fe_{0.8}O_{3-\delta}$ perovskite-type oxygen transport membranes, *J. Europ. Ceram. Soc.* 34 (2014) 3741-3748.

8 J.M. Polfus, W., Xing, G. Pećanac, A. Fossdal, S.M. Hanetho, Y Larring, J. Malzbender, M.-L. Fontaine, R. Bredesen, Oxygen permeation and creep behavior of $Ca_{1-x}Sr_xTi_{0.6}Fe_{0.15}Mn_{0.25}O_{3-\delta}$ (x=0, 0.5) membrane materials, *J. Membr. Sci.* 499 (2016) 172-178.

9 S. Cheng, H. Huang, S. Ovtar, S. B. Simonsen, M. Chen, W. Zhang, M. Søgaard, A. Kaiser, P. V. Hendriksen, C. Chen, High-Performance Microchanneled Asymmetric $Gd_{0.1}Ce_{0.9}O_{1.95-\delta}$–$La_{0.6}Sr_{0.4}FeO_{3-\delta}$-Based Membranes for Oxygen Separation, *ACS Appl. Mater. & Interfaces*, 8 (7) (2016) 4548-4560.

10 . M. Serra, J. Garcia-Fayos, S. Baumann, F. Schulze-Küppers, W.A. Meulenberg, Oxygen permeation through tape-cast asymmetric all-$La_{0.6}Sr_{0.4}Co_{0.2}Fe_{0.8}O_{3-\delta}$ membranes, *J. Membr. Sci.* 447 (2013) 297-305.

11 M. Betz, F. Schulze-Küppers, S. Baumann, W.A. Meulenberg, D. Stöver, Supported oxygen transport membranes or oxyfuel power plants, *Advances Sci. Technol.* 72 (2010) 93-98.

12 J. Sunarso, S. Baumann, J.M. Serra, W.A. Meulenberg, S. Liu, Y.S. Lin, J.C. Diniz da Costa, Mixed ionic–electronic conducting (MIEC) ceramic-based membranes for oxygen separation, *J. Membr. Sci.* 320 (2008) 13-41

13 S. Baumann, F. Schulze-Küppers, S. Roitsch, M. Betz, M. Zwick, E.M. Pfaff, W.A. Meulenberg, J. Mayer, D. Stöver, Influence of sintering conditions on microstructure and oxygen permeation of $Ba_{0,5}Sr_{0,5}Co_{0,8}Fe_{0,2}O_{3-\delta}$ (BSCF) oxygen transport membranes, *J. Membr. Sci.* 359 (2010) 102-109.

14 P. Niehoff, S. Baumann, F. Schulze-Küppers, R.S. Bradley, I. Shapiro, W.A. Meulenberg, P.J. Withers, R. Vaßen, Oxygen transport through supported $Ba_{0,5}Sr_{0,5}Co_{0,8}Fe_{0,2}O_{3-\delta}$ membranes, *Sep. Purif. Technol.* 121 (2014) 60-67.

15 U. Unije, R. Mücke, P. Niehoff, S. Baumann, R. Vaßen, O. Guillon, Simulation of the effect of the porous support on flux through an asymmetric oxygen transport membrane, *J. Membr. Sci.* 524 (2017) 334-343.

16 F.Bouville, E. Maire, S. Meille, B. Van de Moortèle, A. J. Stevensn, Sylvain Deville, Strong, tough and stiff bioinspired ceramics from brittle constituents, *Nat. Mater.* 13 (2014) 508-514.

17 C. Gaudillere, J. Garcia-Fayos, J.M. Serra, Enhancing oxygen permeation through hierarchically-structured perovskite membranes elaborated by freeze-casting, *J. Mater. Chem. A* 2 (2014) 3828-3833.

18 T. Waschkies, R. Oberacker, M.J. Hoffmann, Control of Lamellae Spacing During Freeze Casting of Ceramics Using Double-Side Cooling as a Novel Processing Route, *J. Amer. Ceram. Soc.* 92 (2009) S79-S84.

19 S. Deville, Freeze-Casting of Porous Ceramics: A Review of Current Achievements and Issues, Adv. Eng. Mater. 10 (2008) 155-169.

20 S. Deville, Freeze-Casting of Porous Biomaterials: Structure, Properties and Opportunities, *Mater.* 3 (2010) 1913-1927.

21 Y. Chen, Y. Zhang, J. Baker, P. Majumdar, Z. Yang, M. Han, F. Chen, Hierarchically Oriented Macroporous Anode-Supported Solid Oxide Fuel Cell with Thin Ceria Electrolyte Film, *ACS Appl. Mater. & Interfaces* 6 [7] (2014) 5130-5136.

22 H. Huang, S. Cheng, J. Gao, C. Chen, J. Yi, Phase-inversion tape-casting preparation and significant performance enhancement of $Ce_{0.9}Gd_{0.1}O_{1.95}$–$La_{0.6}Sr_{0.4}Co_{0.2}Fe_{0.8}O_{3-\delta}$ dual-phase asymmetric membrane for oxygen separation, *Mater. Letters* 137 (2014) 245-248.

23 X. Shao, Dehua Dong, G. Parkinson C.-Z. Li, A microchanneled ceramic membrane for highly efficient oxygen separation, *J. Mater. Chem. A* 1 (2013), 9641.

24 R.I. Tomov, M. Krauz, J. Jewulski, S.C. Hopkins, J.R. Kluczowski, D.M. Glowacka, B.A. Glowacki, Direct ceramic inkjet printing of yttria-stabilized zirconia electrolyte layers for anode-supported solid oxide fuel cells, *J. Power Sources* 195 (2010) 7160-7167.

25 O. Ravkina, T. Klande, A. Feldhoff, Investigation of Zr-doped BSCF perovskite membrane for oxygen separation in the intermediate temperature range, J. Solid State Chem. 201 (2013) 101-106.

26 M. Meffert, P. Müller, H.Störmer, L.-S. Unger, C. Niedrig, S.F. Wagner, S. Saher, H.J.M. Bouwmeester, E. Ivers-Tiffée, D. Gerthsen, Effect of yttrium (Y) and zirconium (Zr) doping on the thermodynamical stability of the cubic $Ba_{0,5}Sr_{0,5}Co_{0,8}Fe_{0,2}O_{3-\delta}$ phase, *Microsc. Microanal.* 20 (2014) 466-467.

27 S. E. Naleway, K. C. Fickas, Y. N. Maker, M. A. Meyers, J. McKittrick, Reproducibility of ZrO2-based freeze casting for biomaterials, Mater. Sci. Eng.: C 61 (2016) 105-112.

28 W. Deibert, M.E. Ivanova, W.A. Meulenberg, R. Vaßen, O. Guillon, Preparation and sintering behaviour of $La_{5.4}WO_{12-\delta}$ asymmetric membranes with optimised microstructure for hydrogen separation *J. Membr. Sci.* 492 (2015) 439-451.

29 L. Feldkamp, L. Davis, J. Kress, Practical cone-beam algorithm, *J. Opt. Soc. Am. A* 1 (1984) 612-619.

30 S. Engels, Dissertation, RWTH-Aachen University, Germany 2012.

31 C. Niedrig, C.-Y. Yoo, W. Menesklou, S. Baumann, S.F. Wagner, H.J.M. Bouwmeester, E. Ivers-Tiffée, Electroceramics-XIII, Enschede, 2012.

32 W.K. Hong, G.M. Choi, Oxygen permeation of BSCF membrane with varying thickness and surface coating, *J. Membr. Sci.* 346 (2010) 353-360.

33 H.J.M. Bouwmeester, A. J. Burgraaf, Dense ceramic membranes for oxygen separation, in: A. J. Burgraaf, L. Cot (Eds.), Fundamentals of Inorganic membrane Science and Technology, Elsevier, Amsterdam (1996) 435-528.

34 S. Baumann, P. Niehoff, F. Schulze-Küppers, M. Ramasamy, W. A. Meulenberg, O. Guillon, The Role of Solid-Gas Electrochemical Interfaces for Mixed Ionic Electronic Conducting Oxygen Transport Membranes, *ECS Transactions* 66 [2] (2015) 21-33.

35 W.J. Koros, Y.H. Ma, T. Shimidzu, Terminology for membranes and membrane processes, Pure *Appl. Chem.* 68 [7] (1996) 1479-1489.

36 Z. Shao, W. Yang, Y. Cong, H. Dong, J. Tong, G. Xiong, Investigation of the permeation behavior and stability of a $Ba_{0.5}Sr_{0.5}Co_{0.8}Fe_{0.2}O_{3-\delta}$ oxygen membrane, *J. Membr. Sci.* 172 (2000) 177-188.

37 B. Tjaden, J. Lane, P.J.Withers, R.S. Bradley, D.J.L. Brett, P.R. Shearing, The application of 3D imaging techniques, simulation and diffusion experiments to explore transport properties in porous oxygen transport membrane support materials, *Solid State Ionics* 288 (2016) 315-321.

38 J.Seuba, S. Deville, C. Guizard, A.J. Stevenson, Gas permeability of ice-templated, unidirectional porous ceramics, *Sci. Technol. Adv. Mater.* 17 [1] (2016) 313-323.

39 S. Deville, E.Maire, A. Lasalle, A. Bogner, C. Gauthier, J.Leloup, C. Guizard, In Situ X-Ray Radiography and Tomography Observations of the Solidification of Aqueous Alumnia Particle Suspension – Part I: Initial Instants, *J. Am. Ceram. Soc.* 92 (2009) 2489-2496.

40 S. Wang, W.M. Worek, W.J. Minkowycz, Performance comparison of the mass transfer models with internal reforming for solid oxide fuel cell anodes, *Int. J. Heat Mass. Tran.* 55 (2012) 3933-3945.

41 N. Epstein, On tortuosity and tortuosity Factor in Flow and Diffusion through Porous-media, *Chem. Eng. Sci.* 44 (1989) 777-779.

42 D.K. Edwards, V.E. Denny, A.F. Mills, Transfer Processes: An Introduction to Diffusion and Radiation, 2nd Edition, Hemisphere Publishing (1979).

43 C. Edelmann, Vakuumphysik, Spektrum Akademischer Verlag, Heidelberg/Berlin (1988).

44 A.F. Ismail, K.C. Khulbe, T. Matsuura, Gas Separation Membranes: Polymeric and Inorganic, Springer International Publishing (2015).

45 A. Bareggi, E. Maire, A. Lasalle, S. Deville, Dynamics of the Freezing Front During the Solidification of a Colloidal Alumina Aqueous Suspension: In Situ X-Ray Radiography, Tomography, and Modeling, *J. Am. Ceram. Soc.* 94 (2011) 3570-3578.